Seasonal predictability of extratropical storm tracks in GFDL's high-resolution climate prediction model

Xiaosong Yang*[1,3], Gabriel A. Vecchi[1,2], Rich G. Gudgel[1], Thomas L. Delworth[1,2], Shaoqing Zhang[1], Anthony Rosati[1], Liwei Jia[1,3], William F. Stern[1], Andrew T. Wittenberg[1], Sarah Kapnick[2], Rym Msadek[1,3], Seth D. Underwood[4], Fanrong Zeng[1], Whit Anderson[1], Venkatramani Balaji[1,2]

[1] *NOAA/Geophysical Fluid Dynamics Laboratory,Princeton, New Jersey*

[2] *Atmospheric and Oceanic Sciences Program,Princeton University, Princeton, New Jersey*

[3] *University Corporation for Atmospheric Research, Boulder, Colorado*

[4] *Dynamics Research Corporation, Andover, Massachusetts*

For submission to *Journal of Climate*

July 16, 2014

* *Corresponding author address:* Xiaosong Yang, NOAA/Geophysical Fluid Dynamics Laboratory, 201 Forrestal Rd., Princeton, NJ, 08540

E-mail: Xiaosong.Yang@noaa.gov

ABSTRACT

The seasonal predictability of extratropical storm tracks in Geophysical Fluid Dynamics Laboratory (GFDL)'s high-resolution climate model has been investigated using an average predictability time analysis. The leading predictable components of extratropical storm tracks are ENSO-related spatial pattern for both boreal winter and summer, and the second predictable components are mostly due to changes in external radiative forcing and multidecadal oceanic variability. These two predictable components for both seasons show significant correlation skill for all leads from 0 to 9 months, while the skill of predicting the boreal winter storm track is consistently higher than that of the austral winter. The predictable components of extratropical storm tracks are dynamically consistent with the predictable components of the upper troposphere jet flow for the both seasons. Over the region with strong storm track signals in North America, the model is able to predict the changes in statistics of extremes connected to storm track changes (e.g., extreme low and high sea level pressure and extreme 2m air temperature) in response to different ENSO phases. These results point towards the possibility of providing skillful seasonal predictions of the statistics of extratropical extremes over land using high-resolution coupled models.

1. Introduction

The midlatitude storm tracks are regions of frequent baroclinic waves and associated surface cyclones and anticyclones. These storms are characterized by strong winds and heavy precipitation, and all are thus a source of extreme regional weather and climate events. Additionally, the poleward transport of heat, momentum and moisture associated with midlatitude storms is a prominent part of the global circulation system. Thus, predicting and projecting future changes of storm tracks is of huge societal and scientific interest.

Mid-latitude storm tracks vary on seasonal, interannual and decadal-to-centennial time scales (Chang et al. 2002, 2013a; Stockdale et al. 2011). On interannual timescales, storm tracks change in response to the El Niño-Southern Oscillation (ENSO) cycle. During El Niño years, the Pacific storm track shifts equatorward and downstream (Straus and Shukla 1997; Zhang and Held 1999; Eichler and Higgins 2006), while La Niña events drive a shift in the opposite direction. The dynamics of the midlatitude storm tracks' response to ENSO involve extratropical response to local enhancement of the Hadley circulation over the eastern Pacific (Bjerknes 1969), and there are feebacks from ENSO-induced storm track changes that play an important role in controlling the extratropical response to ENSO (Held et al. 1989). The Northern Hemisphere winter storm tracks also exhibit interdecadal variations (Chang and Fu 2002). On centennial timescales, the CMIP3 and CMIP5 models, project poleward migration and intensification of the Southern Hemisphere storm tracks in the 21^{th} century in response to green house gas changes (Chang et al. 2013a, 2012). The observational, theoretical and modeling aspects of the midlatitude storm tracks on multiple time scales have been extensively studied in the literature (see the review paper by Chang et al. (2002)), but, what has not been assessed as broadly is the extent to which the dynamical prediction system can predict seasonal storm track variations.

State-of-the-art dynamical seasonal prediction systems have demonstrated skill in forecasting oceanic, land surface temperature and precipitation in the retrospective forecasts (e.g., (Saha et al. 2006; Jia et al. 2014)), and the routine seasonal forecasts using dynamical climate models have been provided to society and policy makers among the worldwide operational forecasting centers (Saha et al. 2006, 2014; Merryfield and Coauthors 2013; Stockdale et al. 2011). The useful products derived from the seasonal forecasts have been limited to the first moment of variables of interest, such as the seasonal mean land surface temperature and precipitation, but the predictability of the second moment of variables of interest, such as the variance statistics of extratropical storm tracks, has not been explored. The second moment of a variable contains detailed distribution beyond the simple mean, especially for the information related to extreme climate and weather events. Assessment of the predictability of the second moment statistics would potentially enrich the seasonal forecast information from a single mean to higher order and therefore provide more detailed information for the users. In addition, examining the storm track predictability is a measure of model fidelity, since storm tracks are symbiotically linked to the planetary-scale flow (Cai and Mak 1990). In this study, we evaluate the predictability of extratropical storm tracks in GFDL's high-resolution seasonal prediction system, which has been shown to provide skillful seasonal forecasts of land surface temperature and precipitation (Jia et al. 2014), tropical cyclones (Vecchi et al. 2014), and Arctic sea-ice extent (Msadek et al. 2014a).

In this study, we employ a method, called the average predictability time (APT) optimization (DelSole and Tippett 2009a,b; DelSole et al. 2011), to identify the predictable patterns of storm tracks in the seasonal hindcasts. The APT has been used for identifying an internal interdecadal predictable pattern of sea surface temperature in GFDL's decadal hindcasts (Yang et al. 2013), and is capable of distinguishing the ENSO-driven seasonal signals from anthropogenic forced response of land surface temperature in GFDL's seasonal hindcasts (Jia et al. 2014). Our main goals are to identify the predictable patterns of storm tracks in the hindcasts using APT, assess the prediction skill of those patterns and to understand the mechanisms responsible for that predictability. Details of the hindcasts and observational datasets are discussed in section 2. The methodology is reviewed in section 3. In section 4, the predictable patterns for storm tracks are identified by APT analysis, the retrospective prediction skill is assessed using observations, and the role of mean flow predictability in storm track prediction is investigated. Conclusions and discussions are given in section 5.

2. Model, Hindcast experiments and Observations

The high-resolution climate model explored here, GFDL-FLOR (Forecast-oriented Low Resolution version of GFDL-CM2.5), is a combination of two previously described GFDL coupled model configurations, namely CM2.1 (Delworth et al. 2006) and CM2.5 (Delworth et al. 2012). The atmosphere and land models have an approximately 50km by 50km spatial resolution, and are those used in GFDL-CM2.5 (Delworth et al. 2012), which have ocean models at a $0.25° \times 0.25°$ resolution. The ocean and sea ice components of the model are at $1° \times 1°$ resolution, based on those of GFDL-CM2.1, which has been used extensively for climate research, predictions and projections for close to a decade. In this climate model, the ocean component has been slightly altered from that of CM2.1 by incorporating a newer, higher order advection scheme; an updated parameterization for eddies (Farneti et al. 2010); and a more realistic representation of the solar absorption by the ocean. The resulting model, FLOR, has most of its computational expense and resolution concentrated in the atmosphere and land components. A detailed description of the FLOR model can be found in Vecchi et al. (2014) and Jia et al. (2014).

The seasonal hindcasts were initialized using the GFDL's ensemble coupled data assimilation (ECDA) system. The ECDA employs an ensemble-based filtering algorithm applied to the GFDL-CM2.1. More details of ECDA can be found in Zhang et al. (2007) and Zhang and Rosati (2010). The ECDA covers the period 1960 to present and is being updated monthly for GFDL's seasonal-to-decadal experimental forecasts (Yang et al. 2013; Vecchi et al. 2013; Msadek et al. 2014b). A comprehensive assessment of the 1960-2010 oceanic variability in the latest version of the ECDA can be found in Chang et al. (2013b). As the data assimilation system for FLOR is under development, the initial conditions for the ocean and ice components of the FLOR hindcasts are taken from the ECDA, while the initial conditions for the atmosphere and land components are taken from FLOR atmosphere-only simulations driven by observed SSTs. The 12-member ensemble seasonal hindcasts were initialized on the 1^{st} day every month from 1982 to 2014 and integrated for 12 months with temporally varying anthropogenic and natural forcing. The seasonal hindcast anomalies for each variable were obtained by subtracting out the lead-time dependent climotology from hindcasts. For the historical forcing simulations, the 5 ensemble members using FLOR were integrated using temporally varying anthropogenic and natural forcing from 1860 to 2013. Note that the temporally varying anthropogenic and natural forcings between 1982 to 2014 are exactly the same for the historical forcing simulations and seasonal hindcasts.

The observational data used in this study are the sea level pressure (SLP), 2-meter air temperature, 10-meter wind speeds, 300-hPa zonal winds and precipitation from the ERA-Interim reanalysis of the European Center for Medium-Range Weather Forecasts (ECMWF) (Dee et al. 2011). The NINO3.4 index, the average SST anomaly in the region bounded by 5°N to 5°S and from 170°W to 120°W, is calculated from the United Kingdom Meteorological Office Hadley Centre's Global sea-Ice coverage and SST (HadISST 1.1) analyses (Rayner et al. 2003). A rainy day is defined as a day with the daily precipitation exceeding 1 mm per day based on the WMO recommendation (Klein Tank et al. 2009).

The statistical significance test of the anomaly correlation coefficients (ACC) between observations and hinscasts is formed by the null hypothesis that ACC is 0, and we perform this test by determining whether the confidence interval for ACC contains 0. If the 95% confidence interval for ACC does not contain 0, we conclude that ACC is significant at 5% significant level.

3. Review of Methodology

a. *Storm track statistics*

To highlight synoptic time-scale variability, seasonal standard deviation statistics are computed using a 24-hour difference filter (Wallace et al. 1988), as follows:

$$std = \sqrt{\frac{1}{N}\sum_{t=1}^{N}\left[v(t+24hr) - v(t)\right]^2}, \tag{1}$$

where N is the sample size of each season, and v is a variable representing the storm track activity. As discussed in previous studies (Chang and Fu 2002), this filter has half power point at periods of 1.2 and 6 days, and results obtained based on this filter are very similar to those obtained using other commonly used band-pass filters. Many different variables are commonly used to measure storm-track activity, e.g., the meridional winds in different vertical levels, 500-hPa geopotential height and SLP (Chang et al. 2002, 2012). Here we use SLP for computing the storm track statistics, since our interest is in the surface storm tracks. We compute the seasonal storm track indices using (1) from 6-hourly SLP for both model hindcasts and ERA-Interim reanalysis. We only focus on the winter seasons of December, January and February (DJF) for the northern hemisphere and July, August and September (JAS) for the southern hemisphere. Instead of using conventional June, July and August (JJA) months representing the southern hemisphere winter, JAS is used due to its stronger split jet mean flow than JJA (Yang and Chang 2006) and its stronger field significance of ENSO-teleconnected global temperature and precipitation patterns than JJA (Yang and DelSole 2012).

b. *The average predictability time analysis*

We employ the average predictability time (APT) optimization method to identify characteristic patterns of predictable components in the seasonal hindcasts. Complete details of

APT can be found in DelSole and Tippett (2009a,b). Briefly, the method is to maximize APT, which is defined as the integral over lead time of the "signal to total" variance ratio of a forecast model

$$APT = 2\int_0^\infty \frac{\sigma^2_{signal}(\tau)}{\sigma^2_{total}} d\tau, \tag{2}$$

where $\sigma^2_{signal}(\tau)$ is the variance of the ensemble mean at fixed lead time τ, and σ^2_{total} is the corresponding total variance of the forecast ensemble. For the ensemble forecasts, the signal and total covariance can be approximated by the corresponding ensemble covariances. Following DelSole and Tippett (2009a), maximizing APT in ensemble forecasts leads to the generalized eigenvalue problem

$$\left(2\sum_{\tau=1}^{L} \mathbf{\Sigma}_{signal}(\tau)\right)\mathbf{q} = \lambda \mathbf{\Sigma}_{total}\mathbf{q}, \tag{3}$$

where L is the maximum forecast lead time, $\mathbf{q}$ is the desired projection vector, $\mathbf{\Sigma}_{signal}(\tau)$ is the ensemble mean covariance matrix at the forecast lead time τ, and $\mathbf{\Sigma}_{total}$ is the total ensemble covariance matrix. The eigenvectors $\mathbf{q}$ provide the basis for decomposing the multivariate time series into a complete, uncorrelated set of components ordered such that the first maximizes APT, the second maximizes APT subject to being uncorrelated with the first, and so on. The eigenvalues of (3) correspond to the APT values of each component. This decomposition based on APT is analogous to Empirical Orthogonal Function (EOF) analysis, except that we decompose predictability instead of decomposing variance.

For solving the APT optimization problem (3) in practice, the data are first projected onto the leading principal components (PCs) (DelSole et al. 2011). We have a relatively long sample size of 3960 (i.e., 33 initial conditions, 12 ensemble members and 10 lead times), so the time series and patterns from APT are virtually independent of the number of PCs in the range of 20-40 PCs (not shown). We choose 30 PCs for displaying results for both SLP and 300-hPa zonal wind in the following.

Following DelSole et al. (2011), the statistical significance test of APT was estimated by Monte Carlo methods. The null hypothesis for the test is that the data are drawn from a white noise process. Accordingly, we generated a 30×3960 data matrix by drawing independent random numbers from a normal distribution with zero mean and unit variance. The time dimension of the data was grouped as a set of 30 separate 10-season forecasts with 12 ensemble members each. 30 APT values were then determined. This procedure was repeated 1000 times to generate 1000×30 APT values. The 95^{th} percentile of the 1000×30 APT values was then determined as the threshold values for statistical significance.

4. Results

a. Mean flow and storm track climatology

Since mid-latitude storm tracks interact with the large-scale mean flow through the wave-mean flow interactions, we first examine the model's capability of reproducing the observed climatological mean flow and storm tracks. Fig. 1 shows mean 300-hPa zonal winds for DJF and JAS in observation and FLOR hindcasts. The pattern anomaly correlation coefficent and root mean square error between hindcasts and observation are 0.98 and 2.6 m s^{-1} respectively for DJF, and 0.98 and 2.8 m s^{-1} respectively for JAS. The high spatial correlation coefficients indicate that the model is able to reproduce the geographic feafures of the observed climatological storm tracks in both seasons. Compared to observations, the hindcasts reasonably simulate the location and intensity of the North Africa-East Asia jet, the North Pacific jet, and the North Atlantic jet in the DJF season. The remarkable zonal asymmetry of the DJF jet intensity in the Southern Ocean (i.e., the weaker jet stream in the South Pacific and the stronger jet in the South Indian and South Atlantic Ocean), is well reproduced in the hindcasts. In the JAS season, the model reproduces the observed location and intensity of jets in the North Pacific and the North Atlantic. It is worth noting that the split structure of the Southern Hemisphere winter jet is faithfully reproduced by the model (i.e., the model reproduces the strong subtropical jet extending from the central South Indian Ocean across Australia to the east-central South Pacific Ocean between 20°S and 40°S the polar front jet concentrated along 60°S in the South Pacific and a zone of weak westerlies centered in the New Zealand).

Fig. 2 shows mean storm tracks for DJF and JAS in observation and FLOR hindcasts. The spatial root mean square errors between hindcasts and observation are 0.5 and 0.9 hPa for DJF and JAS respectively. The spatial anomaly correlation coefficents between hindcasts and observation are 0.99 and 0.98 for DJF and JAS respectively, suggesting the high agreement between these two climatological fields. In the DJF season, the location, orientation and intensity of the North Pacific, the North American, the North Atlantic, Eurasia continent as well as Southern Hemisphere storm tracks are well simulated by the model, although the maxima of the North Pacific, the North Atlantic and the South Pacific storm tracks in the model are generally weaker than those in observations. In the JAS season, consistent with reproducing the split jet seen in Fig. 1, the model is capable of reproducing the observed location and intensity of the South Atlantic and southern Indian Ocean storm tracks and the poleward migration of the South Pacific storm tracks.

b. Predictable patterns of Storm tracks

We first apply APT analysis to the storm tracks for the DJF and JAS seasons. The APT values for the two seasons are shown in Fig. 3. Based on the Monte Carlo statistical test described in Section 3b, the first 3 components have statistically significant APT values for DJF and JAS respectively. However, only the two leading components have multi-season predictive skill verified against observations, so we only focus on the two leading components in this study.

1) The DJF season

The component with the maximum APT for the DJF season is shown in Fig 4a. The pattern generally shows an equatorward shift of the north Pacific and north Atlantic storm tracks, the south Atlantic and Indian ocean storm tracks, weakening of the north America and the south Pacific storm tracks. Note that the amplitudes of the pattern are considerably large in the North America (over 0.7 hPa). The APT value for this component is 14.7 months, and the fraction of global variance explained by this component is about 7.8% (Fig. 3). The spatial distribution of the fraction of variance explained by the leading component is shown in Fig. 4b. We see that the leading predictable component explains as much as 35% of the variance in the North America, and 15% of the variance in the Southern Atlantic and Pacific Oceans. These results show that the leading predictable components explain a significant amount of variance in certain geographic locations.

The time series of the leading APT as a function of initialized years from 1982 to 2014 are shown in Fig. 4c for lead times 1-5 and 6-10 respectively. To assess the forecast skill of the component, we project the ERA-Interim data onto the eigenvector $\mathbf{q}$ with maximum APT from (3) to obtain the observed time series, which are indicated by the solid black line in Fig. 4c. The observed time series is highly correlated with the observed NINO3.4 index with the correlation coefficient of 0.79, suggesting this pattern is ENSO-related. The anomaly correlation coefficients (ACC) between forecasts and observations as a function of initial months, shown in Fig. 4d, generally decrease with the lead time, but are statistically significant up to 9 months of lead time at 5% significance level. The skill of predicting this storm track pattern is generally lower than the skill of predicting ENSO itself (Fig. 4c), but they have a similar pattern over the initial months, i.e., the sharp decrease of ACC starting from early summer (June) to early Spring (March) initial conditions. The decrease in predictability over the summer is consistent with the known "spring barrier" of predicting ENSO and ENSO-related land temperature and precipitation patterns (Barnston et al. 2012; Jia et al. 2014).

The leading predictable pattern of the storm track variability is consistent with the ENSO-teleconnected storm track patterns reported in previous modeling and observational studies (Straus and Shukla 1997; Zhang and Held 1999; Eichler and Higgins 2006). The advance of this study is that the ENSO-related pattern is not only successfully identified in seasonal hindcasts using APT analysis, but this pattern as a whole may be retrospectively predictable up to 9 months in advance at the 5% significance level in GFDL's fully-coupled high-resolution seasonal forecasting system.

The second predictable component (PrC2) for the DJF seasonal hindcasts, shown in Fig 5a, generally shows a poleward shift and strengthening of the Southern Hemisphere (SH) storm tracks and weakening of the North Atlantic storm tracks. The APT value for this component is 6.4 months, and the fraction of global variance explained by this component is about 2.8%. The spatial distribution of the fraction of variance explained by PrC2 is shown in Fig. 5b. We see that PrC2 explains as much as 12.5% of the variance in the middle and high latitudes of Southern Oceans. These results show that PrC2 explains comparable amount of variance in certain geographic locations with that of PrC1. The time series of this component as a function of initialized years from 1982 to 2014 are shown in Fig. 5c for lead times 1-5 and 6-10 respectively. The ACC between forecasts and observations as a function of initial months, shown in Fig. 5d, are statistically significant up to 10 month of lead time at 5% significance level, but independent of the lead time.

The time series of the PrC2 in the DJF season exhibits a multi-decadal increasing trend in the hindcasts as well as observations (Fig. 5c), and the associated pattern in the SH bears remarkable similarity with the linear trend pattern in FLOR's historical forcing experiment (Fig. 6a), suggesting the signal in the SH is mostly the response to the changes in external radiative forcings. The pattern is also consistent with CMIP5 models' projections of poleward expansion and strengthening of the SH storm track at the surface (Chang et al. 2012). However, the weakening of the North Atlantic storm track is opposite to the linear trend pattern in the historical forcing experiment, and we speculate that it may be linked to the Atlantic Multidecadal Oscillation (AMO) phase transition from cold to warm in the last 30 years, since the warm phase of AMO tends to weaken the North Atlantic storm track (Zhang and Delworth 2007). Thus, both the radiative forcing and multidecadal oceanic variability could contribute to the seasonal predictability of the DJF storm tracks.

2) The JAS season

The pattern of the PrC1 for the JAS seasonal hindcasts, shown in Fig 7a, generally shows a poleward shift of the South Atlantic storm tracks, a tripole structure with weakening of storm track activity between 40°S and 60°S and strengthening between 30°S and 40°S in the South Pacific, and strengthening of storm tracks in the west Antarctic continent. The APT value for this component is 10.5 months, and the fraction of global JAS variance explained by this component is about 5.5%. This component explains as much as 25% of the variance in the South Pacific Ocean (Fig. 7b), suggesting its significant contribution of predictability in certain geographic locations.

The time series of the leading APT mode as a function of initialized years from 1982 to 2014 are shown in Fig. 7c for lead times 1-5 and 6-10 respectively. Like the DJF PrC1, the observed time series of the JAS PrC1 is highly correlated with the observed NINO3.4 index with the correlation coefficient of 0.82, suggesting this pattern is ENSO-related. The ACC between forecasts and observations as a function of lead time, shown in Fig. 7d, generally shows a sharp decrease from June to February initial conditions for both PrC1 and NINO34 index, although they are significant at 5% significance level over all the lead times. Again, it is likely related to the spring barrier of ENSO prediction. Compared with the DJF season, the skill of predicting the PrC1 and ENSO in JAS is consistently lower at each lead time.

The ENSO-related storm track pattern is consistent with the observed Antarctic Dipole mode associated with ENSO (Yuan 2004). Note that the maximum amplitude center of the pattern locates in the zone where the climatological jet and storm tracks are weaker than the surrounding area in the South Pacific (see Fig. 1 and 2), so the leading predictable pattern of the JAS storm track in the SH is distinct from the storm track pattern associated with the leading atmosphere internal mode - the southern annular mode (Yang and Chang 2007).

The second predictable component (PrC2) for the JAS season, shown in Fig. 8a, generally shows a band of increase between 30°S and 70°S in the South Atlantic, South India Ocean and western South Pacific. The APT value for this component is 8.1 months, and the fraction of explained variance by this component is about 4.3%. The time series of this component as a function of initialized years from 1982 to 2014 are shown in Fig. 8b for lead times 1-5 and 6-10 respectively. The time series of the PrC2 in the JAS season exhibits a multi-decadal increasing trend in the hindcasts as well as in the observations. The ACC between hindcasts and observations as a function of initial months, shown in Fig. 8c, are statistically significant at 5% significance level for 6 out of 10 initial months.

The storm track pattern of the JAS PrC2 bears similarity with the linear trend pattern in the historical forcing experiment (Fig. 6b), but the amplitude is much stronger in the hindcasts than the historical forcing experiment, implying that this component is partly the response to the changes in external radiative forcings. In addition, the linear trend in the observed time series of the JAS PrC2 with a slope of 0.3 unit variate per decade is much weaker than the counterpart of the DJF PrC2 with a slope of 0.8 unit variate per decade (Fig. 5b and 8b), resulting in the lower skill of predicting the trend pattern in JAS than DJF.

The above analysis based on APT decomposed predictable components with different time scales and mechanisms for the storm track, i.e., the ENSO-related component on inter-annual scales and the externally-forced trend component on multi-decadal scales, suggesting that both the forced component and the unforced internal variability contribute to seasonal predictions of mid-latitude storm tracks. This is consistent with the fact that seasonal predictions of land 2m air temperature can be attributed to both the forced component and the unforced (i.e., ENSO) component relating to internal variability (Jia et al. 2014).

3) Hindcast for 2013-2014 DJF season

The APT analysis finds features that systematically maximize the average predictability over all lead times, so the identified predictable components (e.g., the ENSO-related component and the multidecadal trend component) tend to persist over multiple seasons. However, there can be years that exhibit skill, even though the drivers of the APT features are not the principal sources of skill, e.g., in non-ENSO years. The 2013-2014 DJF season provides an example of this, as it was not a classic ENSO year and the observed storm tracks over the North America were enhanced (Fig. 9a). In 2013-2014 DJF, there was a pronounced reduction of storm track activity over the North Pacific ocean and the west coast of the United States, and a substantial increase of storm track activity extending from central Canada down to the Midwestern United States. This pattern differs from the classical cold ENSO pattern, and though the nominal NIÑO3 anomalies in 2013-14 winter were cold, it did not exhibit canonical ENSO anomalies in the eastern tropical Pacific. Nevertheless, the FLOR hindcasts initialized on 1^{st} November, 2013 reproduce the principal aspects of the observed storm track anomalies (Fig. 9b), although the ensemble mean amplitudes are much weaker than the observations. The ensemble-mean forecast is compromised of some ensemble members that bear more and others less similarity to observations, with the ensemble mean showing the largest correlation with observation (Fig. 10). However, we show a "best" ensemble member which looks similar to observation by visual inspection in Fig. 9c. This member was able to reproduce the location and extreme amplitudes of the observed storm track anomalies, indicating that the observed extreme anomalies were in the forecast spread. The ability of the ensemble mean to recover the large observed correlation indicates a predictable element to this particular winter's storm tracks, but the ensemble spread indicates that the extreme values involved a stochastic element. To further examine the relationship among forecast ensembles and observation, we plot the anomalies of each member, ensemble mean and observations for one center of positive anomalies over the midwestern North America and the other center of negative anomalies in the North Pacific in Fig. 10. For both locations, the ensemble spreads are quite large while the observed anomalies are within the ensemble spread, suggesting that the uncertainty to the initial conditions is large and a sufficient mount of ensemble size is required for retrieving the signal for this case.

We note that the hindcasts initialized on 1^{st} October 2013 show less agreement with observations, and there is almost no skill for the hindcasts initialized on 1^{st} September 2013 and earlier (not shown). Therefore, the skill for this year was limited to one to two months lead. A more detailed exploration of the mechanisms and sources of the predictability for this case is underway, and including additional experiments will be described in the future.

c. Roles of mean flow in storm track predictability

Mid-latitude storm track variations are symbiotically linked to the planetary-scale flow changes and their associated eddy-mean flow interactions (Cai and Mak 1990; Branstator 1995). The dynamical processes governing ENSO-induced storm track predictability include representing the the planetary-scale flow associated with anomalous tropical heating and the eddy-mean flow interactions (Held et al. 1989). In general, a corresponding shift in the storm track structure will accompany an anomaly in the mean jet flow. We have shown that the ENSO-induced storm track pattern is predictable up to multiple seasons in advance in the GFDL high-resolution prediction system. To further confirm that the predictive skill arises from the consistent dynamical processes associated with the ENSO-induced forcing, we examine the predictable patterns for the 300 hPa zonal winds.

Fig 11a shows the leading predictable pattern of DJF 300 hPa zonal winds. In the tropics, the pattern shows easterly anomalies in the eastern tropical Pacific Ocean and westerly anomalies in the tropical Atlantic Ocean, resembling a Gill-type response to ENSO-induced heating anomalies (Gill 1980; Jin and Hoskins 1995). In the NH subtropics and midlatitudes, the pattern shows a strong dipole with strengthening of the subtropical jet and weakening of the mid-latitude jet extending from the North Pacific across North America to the North Atlantic, reminiscent of the Pacific-North American teleconnection pattern (PNA) (Wallace and Gutzler 1981) in the upper troposphere jet field. The pattern in the South Pacific also shows a strong dipole with strengthening of the subtropical jet and weakening of the mid-latitude jet, while a weak dipole shifting jet equatorward extends from the South

Atlantic to the South India. The APT value for this component is 17.9 months, and the fraction of global variance explained by this component is about 23.8%. The spatial distribution of the fraction of variance explained by this component also shows strong geographic locations, e.g., the fraction is as much as 50% in tropics and subtropics, and 30% in the extropics of North America (Fig. 11b).

The observed and hindcasted time series of the leading APT as a function of initialized years from 1982 to 2014 are shown in Fig. 11c for lead times 1-5 and 6-10 respectively. The observed time series is very strongly correlated with the observed NINO3.4 index with the correlation coefficient 0.96, suggesting this pattern is ENSO-related. The skill of predicting this 300 hPa zonal wind pattern is almost tantamount to the skill of predicting ENSO itself. The second predictable pattern of the DJF 300-hPa zonal wind also exhibits a poleward shift and strengthening of the SH mid-latitude jet (not shown), which is consistent with the PrC2 of the SH storm track.

Fig 12a shows the leading predictable pattern of the JAS 300-hPa zonal winds. In the tropics, the pattern also shows a similar Gill-type response wind pattern to ENSO-induced heating anomalies as the DJF pattern. In the subtropics and midlatitudes,the maximum loadings of the pattern locate in the South Pacific with strengthening of the subtropical jet and the weakening of mid-latitude jet. The patterns in the South Atlantic and South Indian Oceans are generally of opposite signs to that in the South Pacific, although the associated amplitudes are much weaker. The zonal wind pattern is consistent with the observed wavetrain pattern associated with ENSO in the SH winter (Karoly 1989) and the observed Antarctic Dipole mode associated with ENSO (Yuan 2004). The APT value for this component is 15.7 months, and the fraction of global variance explained by this component is about 15.3%. This component explains as much as 50% in certain tropical and subtropical areas, and 30% in the South Pacific (Fig. 12b). Compared to the DJF season, the APT value and the fraction of global variance explained by PrC1 are consistently lower in JAS, suggesting the strong seasonal variations of the ENSO-teleconnected 300-hPa zonal wind predictability.

The observed and hindcasted time series of the leading APT as a function of initialized years from 1982 to 2014 are shown in Fig. 12b for lead times 1-5 and 6-10 respectively. Again, the observed time series is very strongly correlated with the observed NINO3.4 index with the correlation coefficient of 0.91 (Fig. 12b), suggesting this pattern is also strongly ENSO-related. The skill of predicting this 300 hPa zonal wind pattern is generally comparable with the skill of predicting ENSO itself.

In summary, the leading predictable 300-hPa zonal wind patterns are dynamically consistent with the leading storm track patterns reported in Section 4b for both DJF and JAS seasons, and they are all related to ENSO. For instance, in DJF, the equatorward jet shift is accompanied by its storm track shift in the North Pacific, and the jet weakening is associated with a storm reduction in the mid and high latitudes of North America; in JAS season, the jet weakening is consistent with a storm reduction in the zone between subtropical and polar front jets in the South Pacific.

d. *Impact on extreme events*

The increase (reduction) of seasonal storm tracks enhances (reduces) the weather disturbances (both cyclones and anticyclones), so the storm track changes associated with ENSO are characterized by changes in second-moment statistics (e.g., width of distribution) of weather-relevant variables (e.g., SLP, temperature, surface winds and precipitation). Since the ENSO-related storm track patterns are to some extent predictable in the model, we expect the corresponding second-moment statistics changes to be predictable. We use the percentile statistics as a measure of the distribution. Here, we examine the 1^{st}, 50^{th} and 99^{th} percentile values of SLP, temperature, wind and precipitation in the DJF season for 5 year composites of El Niño (1982,1986, 1991, 1997 and 2009) and La Niña (1988, 1999, 2000, 2007 and 2010) respectively. The year here refers to the year of the January.

We focus on the crossline with maximum storm track predictable signals which extends from northwestern Canada to the midwestern USA (Fig. 13a). The 1^{st}, 50^{th} and 99^{th} percentile values of SLP, calculated from the 6-hourly model and ERA-Interim data during the composite El Niño years and La Niña years along the crossline are shown in Fig 13. The model predicts more (less) extreme 99^{th} and 1^{st} percentile values of SLP during La Niña (El Niño) years. The 99^{th} percentile SLP values changing with the ENSO phases are in good agreement between observations and model simulations. The predicted 50^{th} percentile values changing with ENSO agree with observations only in the western half of the crossline, while the predicted 1^{th} percentile values agree with observations only in the eastern half of the crossline. The distribution width changes of SLP associated with ENSO tend to skew to the anticyclone extremes in both the ERA-Interim reanalysis and model hindcasts, especially in the western half of the crossline. Note that the similar changes of extreme percentile values associated with ENSO phases were found in other short lead hindcasts (e.g., initialized later than 1st June of the composite years), and the changes are virtually indistinguishable for the hindcasts initialized earlier than 1st July of the composite years (not shown).

The similar percentile values for the 2-m air temperature (T2m), 10-m wind speed (W10m) and the daily precipitation are shown in Fig 14. The model and observation agree well on the decreased (increased) 50^{th} and 1^{st} percentile values of T2m during La Niña (El Niño) years, while there is no agreement between the model and observation for the 99^{th} percentile values changing with the ENSO phases. For W10m, there is a general agreement between model and observation on the increased (decreased) 50^{th} and 99^{th} percentile values during La Niña (El Niño) years, although the contrast between the two phases of ENSO for 99^{th} percentile values is weaker in observations. The daily precipitation's 99^{th} percentile value changes associated with ENSO phases are in low agreement between model and observation, although the simulated daily precipitation shows a very slight coherent increased (decreased) 99^{th} percentile values during La Niña (El Niño) years. Interestingly, model and observations generally agree on more rainy days during La Niña years than El Niño years (Fig. 15).

The percentile value changes of the meteorological variables associated with the ENSO phases are dynamically consistent with the corresponding predictable storm track changes over North America. During La Niña (El Niño) years, enhanced (reduced) storm tracks correspond to increased (decreased) anticyclones and cyclones over North America, leading to a broader (narrower) distribution width of SLP, i.e., the larger (smaller) 99^{th} percentile values and smaller (larger) 1^{st} percentile values. The distribution width changes of SLP tend to skew to the anticyclone extremes in both the ERA-Interim reanalysis and model hindcasts. Consequently, the distribution width changes of T2m skew to the cold temperature extremes, since an extreme cold event is generally linked to an extreme anticyclone with a cold front on its leading edge. The model also predicts coherent 10-m wind speed, daily precipitation extremes and rainy day ratio changes associated with ENSO. Thus, the high-resolution model is capable of providing the extreme-related second-order statistical information beyond a single mean for seasonal forecasts.

5. Conclusions

The seasonal predictability of extratropical storm tracks in GFDL's high-resolution seasonal hindcasts has been investigated using APT analysis. For both DJF and JAS seasons, the leading predictable storm track patterns are ENSO-related. The positive phase of the DJF pattern generally shows an equatorward shift of the North Pacific and North Atlantic storm tracks, as well as of the South Atlantic and Indian ocean storm tracks, and weakening of the North America and the South Pacific storm tracks. Over 1980-2013, the whole pattern is retrospectively predictable up to 9 months in advance at the 5% significance level. The positive phase of the JAS pattern is characterized by a poleward shift of the South Atlantic storm tracks, a dipole structure with weakening of storm track activity between 40°S and 60°S and strengthening between 30°S and 40°S in the South Pacific, and strengthening of storm tracks in the western Antarctic continent. The retrospective predictive skill of the

JAS pattern is generally lower than that of the DJF pattern.

The positive phase of the second predictable component for the DJF seasonal hindcasts generally shows a poleward shift and strengthening of the Southern Hemisphere storm tracks and weakening of the North Atlantic storm tracks. The second mode's time series is dominated by a multi-decadal trend in both hindcasts and observations, corresponding to the response to changes in external forcing and AMO phases. The second predictable component for the JAS season generally shows a band of increased storm activity between 30°S and 70°S in the South Atlantic, South India Ocean and the western part of the South Pacific, and the associated time series is trend-like, although the trend signal is weaker than during the DJF season. The significant role of radiative forcing to the seasonal prediction is also seen in the land surface temperature predictability using the same model (Jia et al. 2014), suggesting seasonal climate prediction is a joint initial-boundary value problem.

The ENSO-related leading predictable storm track component is dynamically consistent with the leading predictable component of the 300-hPa zonal wind during both DJF and JAS seasons. For example, the equatorward jet shift in the DJF predictable mode is accompanied by a similar storm track shift in the North Pacific, while the jet weakening is associated with the storm reduction in the mid and high latitudes of North America; in JAS, the jet weakening has a storm reduction in the zone between the subtropical and polar front jets in the South Pacific.

The fraction of global variance explained by each predictable component for both seasons is generally lower than about 10%, however, the predictable components can explain a substantially large amount of the variance over broad geographic regions. For example, the leading predictable compoment of storm tracks in DJF explains as much as 35% of the variance over much of North America.

The FLOR model was able to retrospectively predict the meteorological variable extreme changes associated with ENSO over the region with the maximum predictable storm track signals in North America (Section 4d). During La Niña (El Niño) years, enhanced (reduced) storm tracks correspond to increased (decreased) anticyclones and cyclones, which lead to a broader (narrower) distribution width of SLP, i.e., the larger (smaller) 99^{th} percentile values and smaller (larger)1^{st} percentile values. The changes in distribution width of SLP tend to skew to the anticyclone extremes in both the ERA-Interim reanalysis and model hindcasts. Consequently, the shape of the probability density of T2m changes so as towards skew to cold temperature extremes, since an extreme cold event is generally linked to an extreme anticyclone. The model also predicts coherent shifts in the statistics of extremes of 10-m wind speed, daily precipitation extremes and rainy day ratio changes associated with ENSO. Hence, as it has been able to do in the tropics when focusing on tropical cyclones (Vecchi et al. 2014), this high-resolution model is capable of providing higher-order statistical information related to extremes , thus enriching the seasonal forecast products for the research community and decision makers beyond the seasonal mean.

The analyzed seasonal predictability of extratropical storm tracks may be subject to the forecast model and the initialization methodology used. Further improvements in predictive skill of extratropical storm tracks are expected when the seasonal prediction system directly uses the FLOR as the data assimilation model.

Acknowledgments.

We thank Lucas Harris and Liping Zhang for helpful reviews of an earlier draft. We thank Isaac Held for insightful discussions about this research which lead to improvements and clarifications. This research was supported by the Visiting Scientist Program at the National Oceanic and Atmospheric Administration's Geophysical Fluid Dynamics Laboratory, administered by the University Corporation for Atmospheric Research. This research was partly supported by the Disaster Recovery Act of 2013.

REFERENCES

Barnston, A. G., M. K. Tippett, M. L. L'Heureux, S. Li, and D. G. DeWitt, 2012: Skill of real-time seasonal ENSO model predictions during 200211: Is our capability increasing?. bull. amer. meteor. soc., 93, 631651. *Bull. Amer. Mereor. Soc.*, **93**, 631–651, doi:10.1175/BAMS-D-11-00111.1.

Bjerknes, J., 1969: Atmospheric teleconnections from the equatorial Pacific. *Mon. Wea. Rev.*, **97**, 163–172.

Branstator, G., 1995: Organization of storm track anomalies by recurring low-frequency circulation anomalies. *J. Atmos. Sci.*, **52**, 207–226.

Cai, M. and M. Mak, 1990: Symbiotic relation between planetary and synoptic scale waves. *J. Atmos. Sci.*, **47**, 2953–2968.

Chang, E., Y. Guo, and X. Xia, 2012: CMIP5 multimodel ensemble projection of storm track change under global warming. *J. Geophys. Res.*, **117**, D23 118, doi:10.1029/2012JD018578.

Chang, E. K. M. and Y. Fu, 2002: Interdecadal variations in northern hemisphere winter storm track intensity. *J. Climate*, **15**, 642–658.

Chang, E. K. M., Y. Guo, X. Xia, and M. Zheng, 2013a: Storm-track activity in IPCC AR4/CMIP3 model simulations. *J. Climate*, **26**, 246–260.

Chang, E. K. M., S. Lee, and K. L. Swanson, 2002: Storm track dynamics. *J. Climate*, **15**, 2163–2183.

Chang, Y.-S., S. Zhang, A. Rosati, T. L. Delworth, and W. F. Stern, 2013b: An assessment of oceanic variability for 1960-2010 from the GFDL ensemble coupled data assimilation. *Clim. Dyn.*, **40**, 775–803, doi:10.1007/s00382-012-1412-2.

Dee, D. P., et al., 2011: The ERA-Interim reanalysis: configuration and performance of the data assimilation system. *Q.J.R. Meteorol. Soc.*, **137**, 553–597.

DelSole, T. and M. K. Tippett, 2009a: Average predictability time. part I: Theory. *J. Atmos. Sci*, **66**, 1172–1187, doi:10.1175/2008JAS2868.1.

DelSole, T. and M. K. Tippett, 2009b: Average predictability time. part II: seamless diagnosis of predictability on multiple time scales. *J. Atmos. Sci.*, **66**, 1188–1204, doi: 10.1175/2008JAS2869.1.

DelSole, T., M. K. Tippett, and J. Shukla, 2011: A significant component of unforced multidecadal variability in the recent acceleration of global warming. *J. Clim.*, **24**, 909–926.

Delworth, T. L., et al., 2006: GFDL's CM2 global coupled climate models. part I: Formulation and simulation characteristics. *J. Clim.*, **19**, 643–674.

Delworth, T. L., et al., 2012: Simulated climate and climate change in the GFDL CM2.5 High-Resolution Coupled Climate Model. *Journal of Climate*, **25**, 2755–2781.

Eichler, T. and W. Higgins, 2006: Climatology and ENSO-Related Variability of North American Extratropical Cyclone Activity. *J. Climate*, **19**, 2076–2093.

Farneti, R., T. L. Delworth, A. J. Rosati, S. M. Griffies, and F. Zeng, 2010: The role of mesoscale eddies in the rectification of the southern ocean response to climate change. *J. Phys. Oceanogr.*, **40**, 1539–1557.

Gill, A. E., 1980: Some simple solutions for heat-induced tropical circulations. *Quart. J. Roy. Meteor. Soc.*, **106**, 447–462.

Held, I. M., S. W. Lyons, and S. Nigam, 1989: Transients and the extratropical response to El Niño. *J. Atmos. Sci.*, **46**, 163–174.

Jia, L., et al., 2014: Improved seasonal prediction skill of land temperature and precipitation in a GFDL high-resolution climate model. *J. Climate*, submitted.

Jin, F. and B. J. Hoskins, 1995: The direct response to tropical heating in a baroclinic atmosphere. *J. Atmos. Sci.*, **52**, 307–319.

Karoly, D. J., 1989: Southern Hemisphere circulation features associated with El Niña-Southern Oscillation events. *Journal of Climate*, **2**, 1239–1252.

Klein Tank, A. M. G., F. W. Zwiers, and X. Zhang, 2009: Guidelines on analysis of extremes in a changing climate in support of informed decisions for adaption. *Climate data and monitoring*, WMO-TD 1500, 56pp, WCDMP-No. 72.

Merryfield, W. J. and Coauthors, 2013: The Canadian Seasonal to Interannual Prediction System. Part I: models and initialization. *Mon. Wea. Rev.*, **141**, 2910–2945.

Msadek, R., G. A. Vecchi, M. Winton, and R. G. Gudgel, 2014a: Importance of initial conditions in seasonal predictions of arctic sea ice extent. *Geophys. Res. Lett.*, submitted.

Msadek, R., et al., 2014b: Predicting a decadal shift in north atlantic climate variability using the gfdl forecast system. *J. Climate*, in press, doi:10.1175/JCLI-D-13-00476.1.

Rayner, N. A., D. E. Parker, E. B. Horton, C. K. Folland, L. V. Alexander, D. P. Rowell, and A. Kaplan, 2003: Global analyses of sea surface temperature, sea ice, and night marine air temperature since the late nineteenth century. *J. Geophys. Res.*, **108 (D14)**, 4407, doi:10.1029/2002JD002670.

Saha, S., et al., 2006: The NCEP Climate Forecat System. *J. Climate*, **19 (15)**, 3483–3517.

Saha, S., et al., 2014: The NCEP Climate Forecast System Version 2. *J. Climate*, **27**, 2185–2208.

Stockdale, T. N., et al., 2011: ECMWF seasonal forecast system 3 and its prediction of sea surface temperature. *Clim. Dyn.*, **37**, 455–471.

Straus, D. M. and J. Shukla, 1997: Variations of midlatitude transient dynamics associated with ENSO. *J. Atmos. Sci.*, **54**, 777–790.

Vecchi, G., et al., 2014: On the seasonal forecasting to regional tropical cyclone activity. *J. Climate*, in press.

Vecchi, G. A., et al., 2013: Multiyear predictions of north atlantic hurricane frequency: Promise and limitations. *Jounral of Climate*, **26**, 5337–5357.

Wallace, J., G. Lim, and M. Blackmon, 1988: Relationship between cyclone tracks, anticyclone tracks and baroclinic waveguides. *J. Atmos. Sci.*, **45**, 439–462.

Wallace, J. M. and D. S. Gutzler, 1981: Teleconnections in the geopotential height field during Northern Hemisphere winter. *Mon. Wea. Rev.*, **109**, 784–812.

Yang, X. and E. K. M. Chang, 2006: Variability of the southern hemisphere winter split flow: A case of two-way reinforcement between mean flow and eddy anomalies. *Journal of the Atmospheric Sciences*, **63**, 634–650.

Yang, X. and E. K. M. Chang, 2007: Eddy-zonal flow feedback in the southern hemisphere winter and summer. *J. Atmos. Sci*, **64**, 3091–3112.

Yang, X. and T. DelSole, 2012: Systematic comparison of ENSO teleconnection patterns between models and observations. *J. Climate*, **25**, 425–446.

Yang, X., et al., 2013: A predictable AMO-like pattern in GFDL's coupled initialization and decadal forecasting system. *Jounal of Climate*, **26**, 650–661.

Yuan, X., 2004: ENSO-related impacts on Antarctic sea ice: a synthesis of phenomenon and mechanisms. *Antarctic Science*, **16**, 415–425, doi:10.1017/S0954102004002238.

Zhang, R. and T. L. Delworth, 2007: Impact of the Atlantic Multidecadal Oscillation on North Pacific climate variability. *Geophys. Res. Lett.*, **34**, L23708, doi:10.1029/2007/GL031601.

Zhang, S., M. J. Harrison, A. Rosati, and A. T. Wittenberg, 2007: System design and evaluation of coupled ensemble data assimilation for global oceanic climate studies. *Mon. Wea. Rev.*, **135**, 3541–3564.

Zhang, S. and A. Rosati, 2010: An inflated ensemble filter for ocean data assimilation with a biased coupled GCM. *Mon. Wea. Rev.*, **138**, 3905–3931.

Zhang, Y. and I. M. Held, 1999: A linear stochastic model of a GCM's midlatitude storm tracks. *J. Atmos. Sci.*, **56**, 3416–3435.

List of Figures

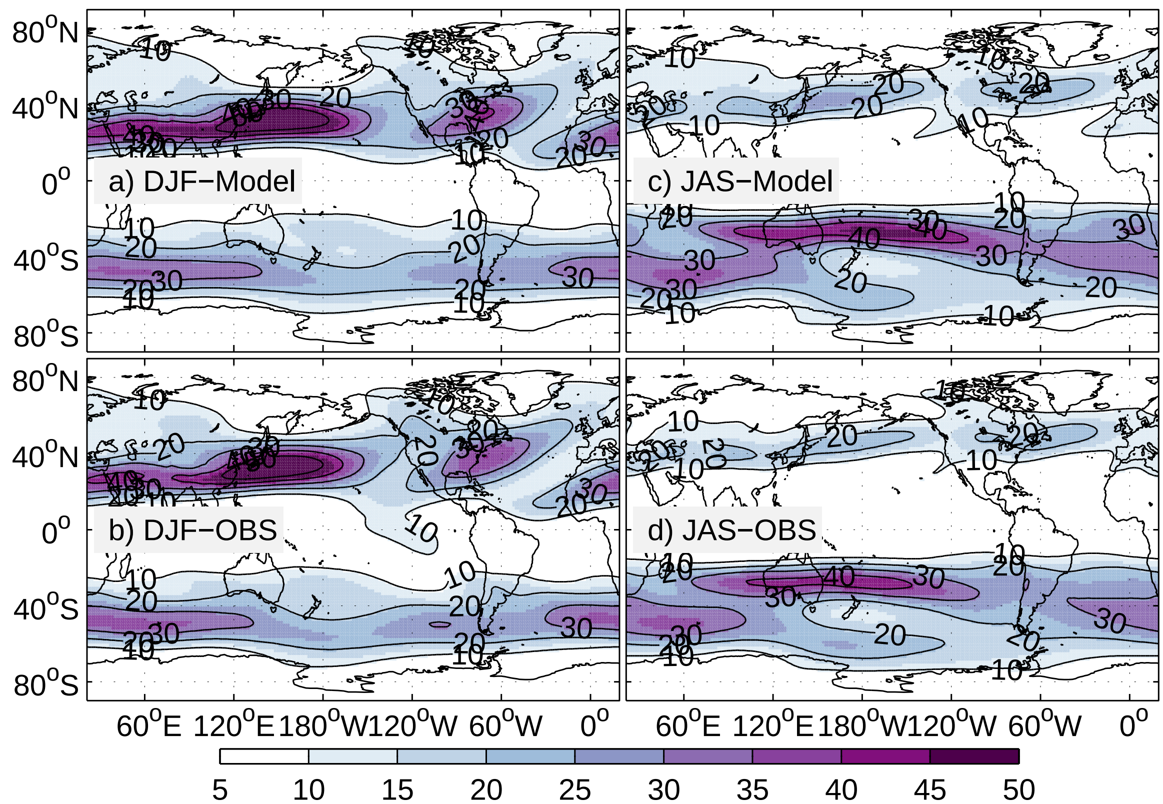

FIG. 1. The climatological 300-hPa zonal winds for DJF in model a) and observation b), and JAS in model c) and observation d). The shading interval is 5 m s^{-1}. Note the model climatology is also averaged over all lead times for displaying purpose.

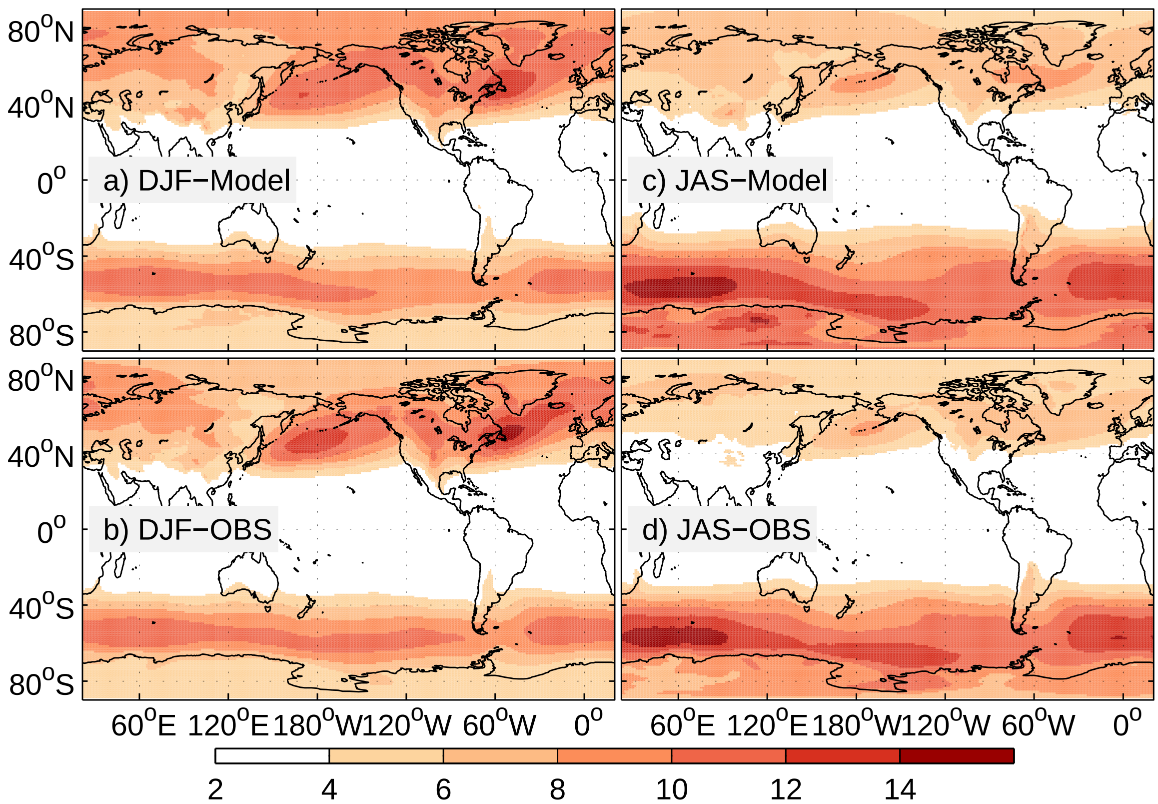

Fig. 2. The climatological storm tracks measured by the standard deviation of 24-hour-difference filtered sea-level-pressures for DJF in model hindcasts a) and observation b), and JAS in model hindcasts c) and observation d). The shading interval is 2 hPa.

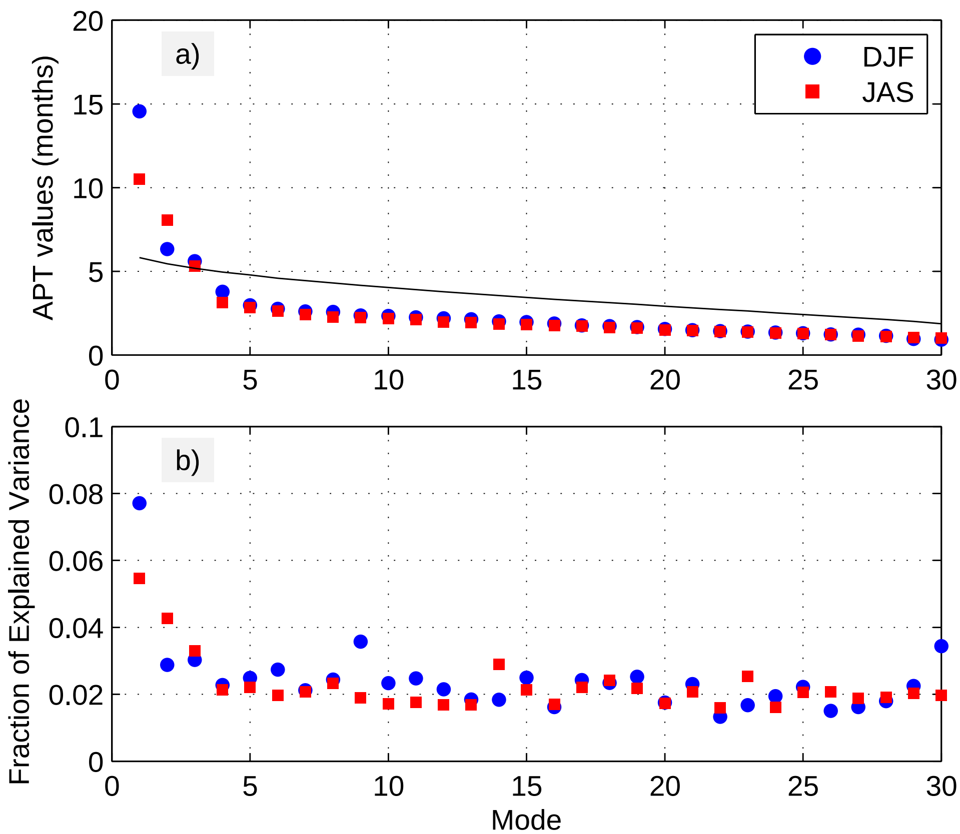

FIG. 3. a) The APT values and b) the associated fraction of explained variance using 30 leading PCs for the 24-hour difference filtered SLP in DJF and JAS. Solid line is the 5% significance level of the APT values.

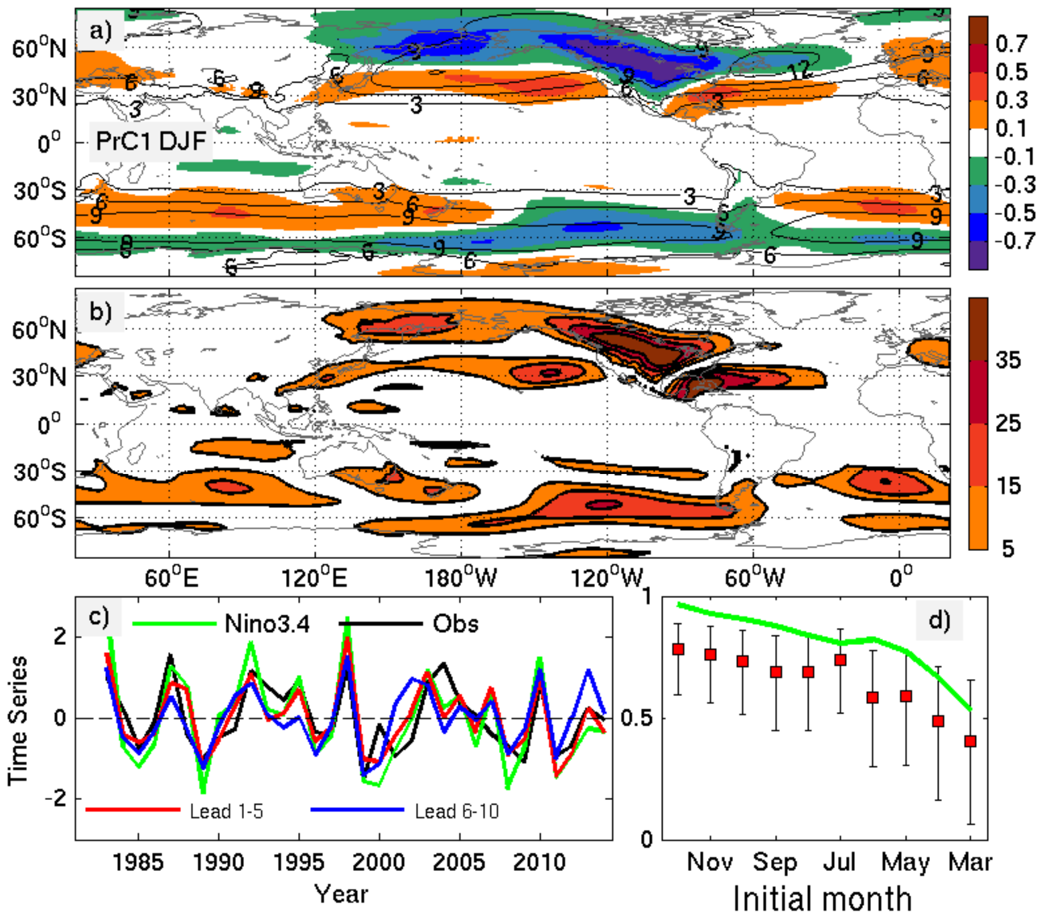

FIG. 4. a) The spatial structure of the predictable component (shading) that maximized the average predictability time of storm tracks in the seasonal hindcasts for the DJF season, which is called PrC1. The black contour denotes the climatological storm tracks (in hPa). The shading unit is hPa per unit standard deviation. b) Percent of variance of storm tracks explained by PrC1. c) The ensemble mean time series of PrC1 averaged over lead time 1-5 months (red solid) and 6-10 months (blue solid) as a function of time, the time series of the ERA Interim data projected onto PrC1 (black solid), and the NINO34 index (green solid) from 1982 to 2014. d) The anomaly correlation coefficients (ACC) between forecasts and observations (red squares) and associated 95% error bars as a function of initial month. The green line denotes the ACC for the NINO34 index.

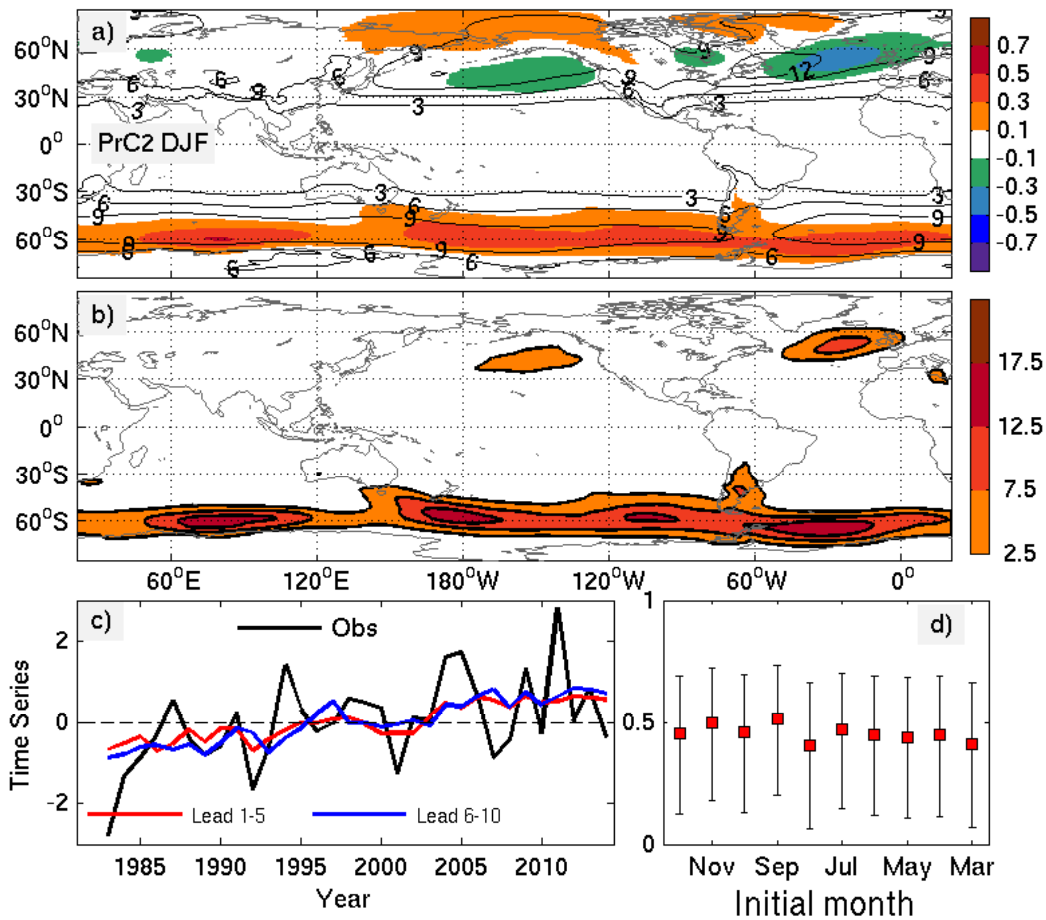

FIG. 5. a) The spatial structure of the second predictable component (shading, in hPa per unit standard deviation) that maximized the average predictability time of storm tracks in the hindcasts for the DJF season, which is called PrC2. The black contour denotes the climatological storm tracks (in hPa). b) Percent of variance of storm tracks explained by PrC2. c) The ensemble mean time series of PrC1 averaged over lead time 1-5 months (red solid) and 6-10 months (blue solid) as a function of time, the time series of the ERA Interim data projected onto PrC1 (black solid). d) The anomaly correlation coefficients (ACC) between forecasts and observations (red squares) and associated 95% error bars as a function of the forecast lead time.

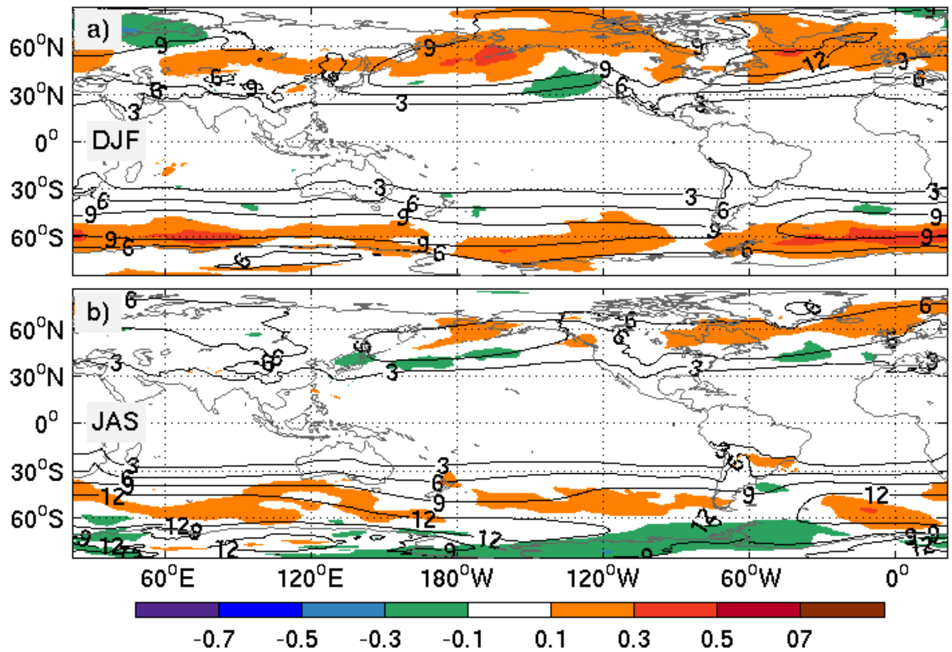

Fig. 6. The linear trend pattern of storm tracks (shading) derived from the 5-member historical forcing simulations of FLOR from 1981 to 2013 for the DJF (a) and JAS (b) seasons. The shading unit is hPa per unit standard deviation. The black contour denotes the climatological storm tracks (in hPa).

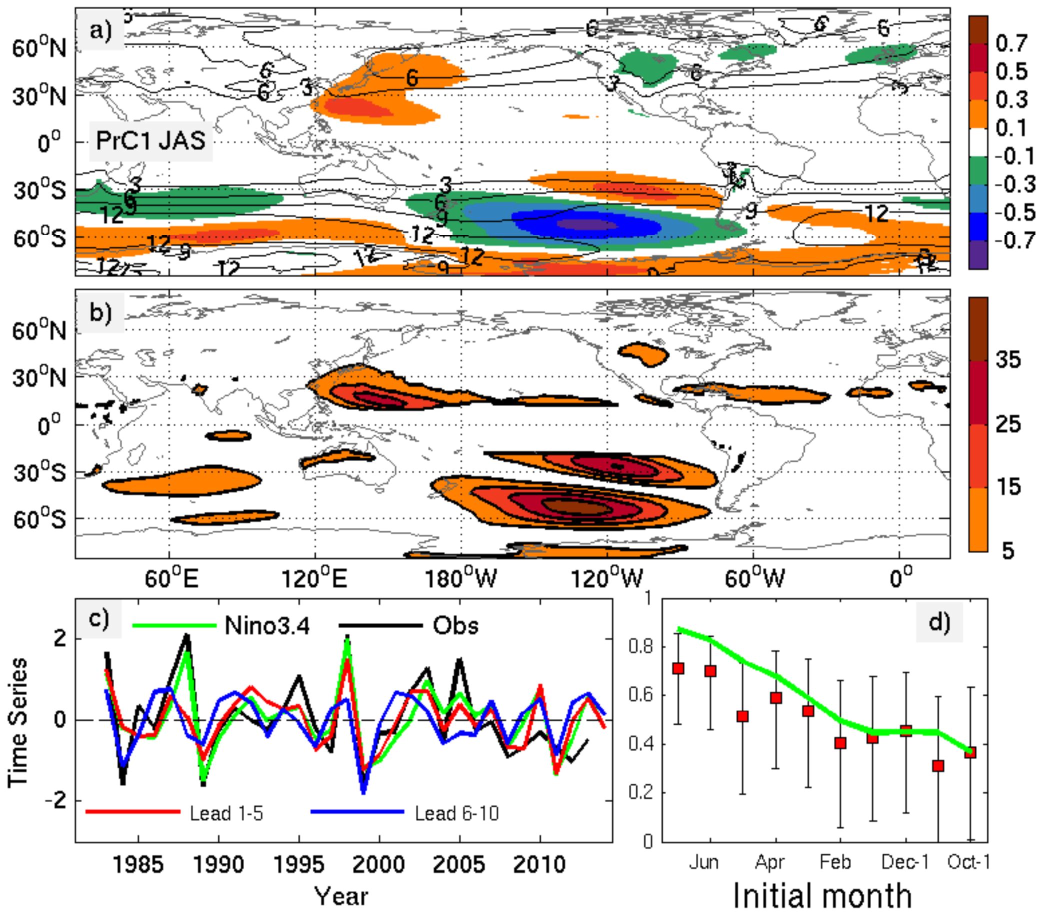

FIG. 7. As in Fig. 4, but for the JAS season.

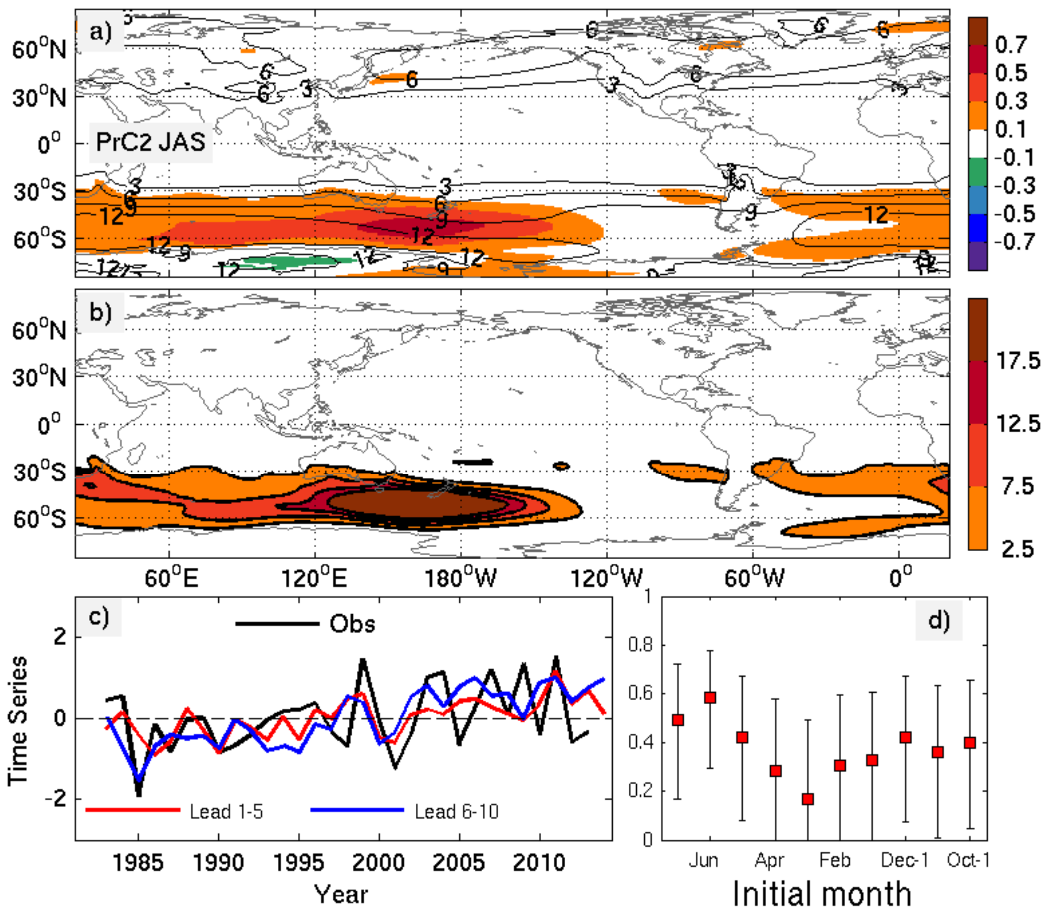

Fig. 8. As in Fig. 5, but for the JAS season.

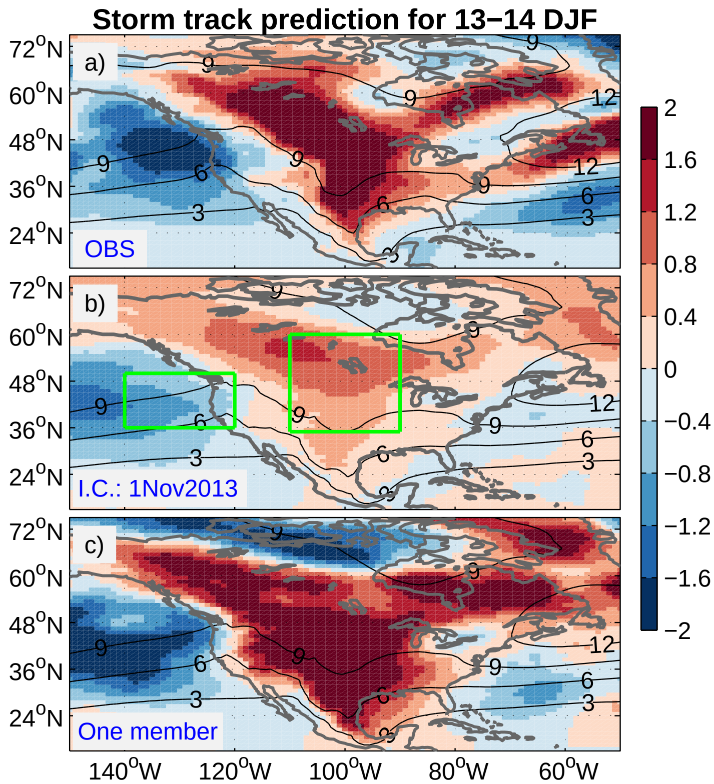

FIG. 9. a) The observed storm track anomalies (shading) for the 2013-2014 DJF season. The ensemble mean b) and one "best" member c) of the predicted storm track anomalies initialized on 1^{st} November 2013. The black contour denotes the climatological storm tracks. Units are hPa.

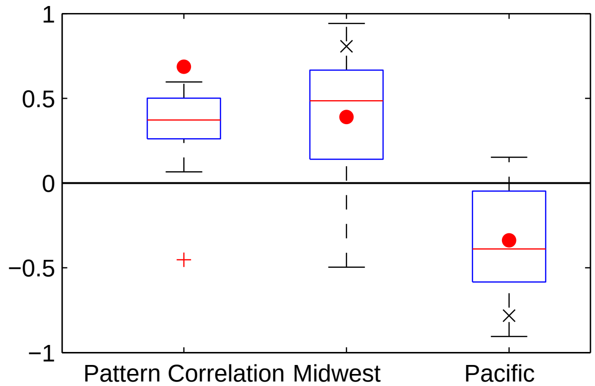

Fig. 10. The box and whisker plots for the pattern correlation coefficients (left column) between each ensemble member and observed storm track anomalies over the North Pacific and North American region (25°N-70°N, 150°W-50°W), the spatial mean storm track anomalies of each ensemble member and ensemble mean for one region (35°N-60°N,110°W-90°W) over the midwestern North America (middle column) and the other (35°N-50°N, 140°W-120°W) in the North Pacific (right column) respectively. The ensemble mean values are denoted as the red cycle symbols, and the observed values are denoted as the black cross symbols. The hindcast is the same as Fig. 9.

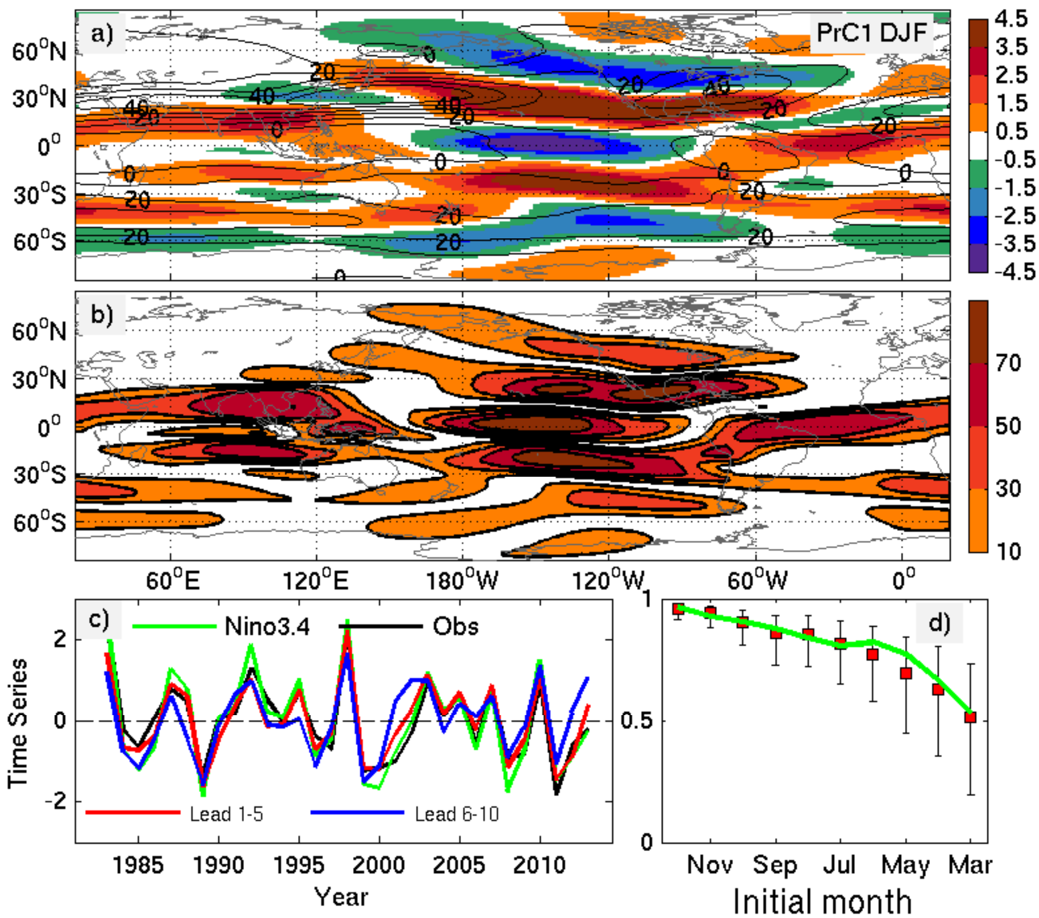

FIG. 11. a) The spatial structure of the leading predictable component (shading) that maximized the average predictability time of 300-hPa zonal winds in the hindcasts for the DJF season, which is called PrC1. The black contour denotes the climatological 300-hPa zonal winds (in m s^{-1}). The shading unit is m s^{-1} per unit standard deviation. b) Percent of variance of storm tracks explained by PrC1. c) The ensemble mean time series of PrC1 averaged over lead time 1-5 months (red solid) and 6-10 months (blue solid) as a function of time, the time series of the ERA Interim data projected onto PrC1 (black solid). d) The anomaly correlation coefficients (ACC) between forecasts and observations (red squares) and associated 95% error bars as a function of the forecast lead time. The green line denotes the ACC for the NINO34 index.

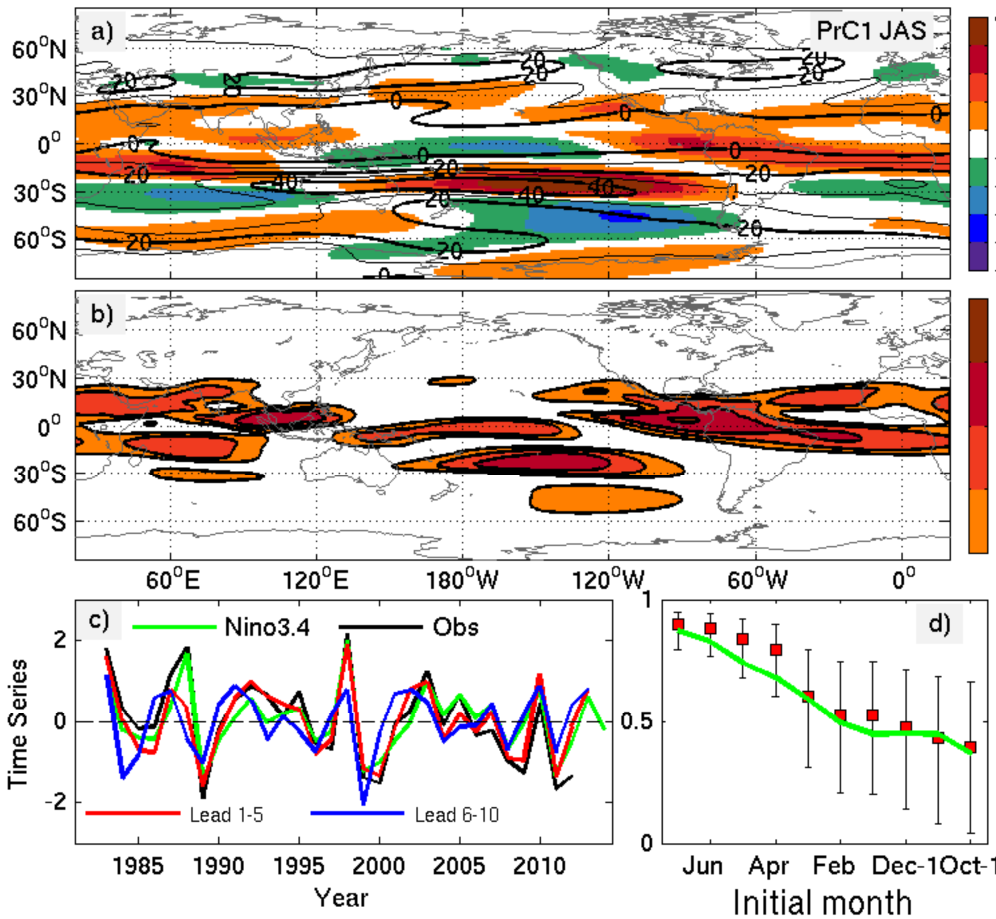

Fig. 12. As in Fig. 11 but for the JAS season.

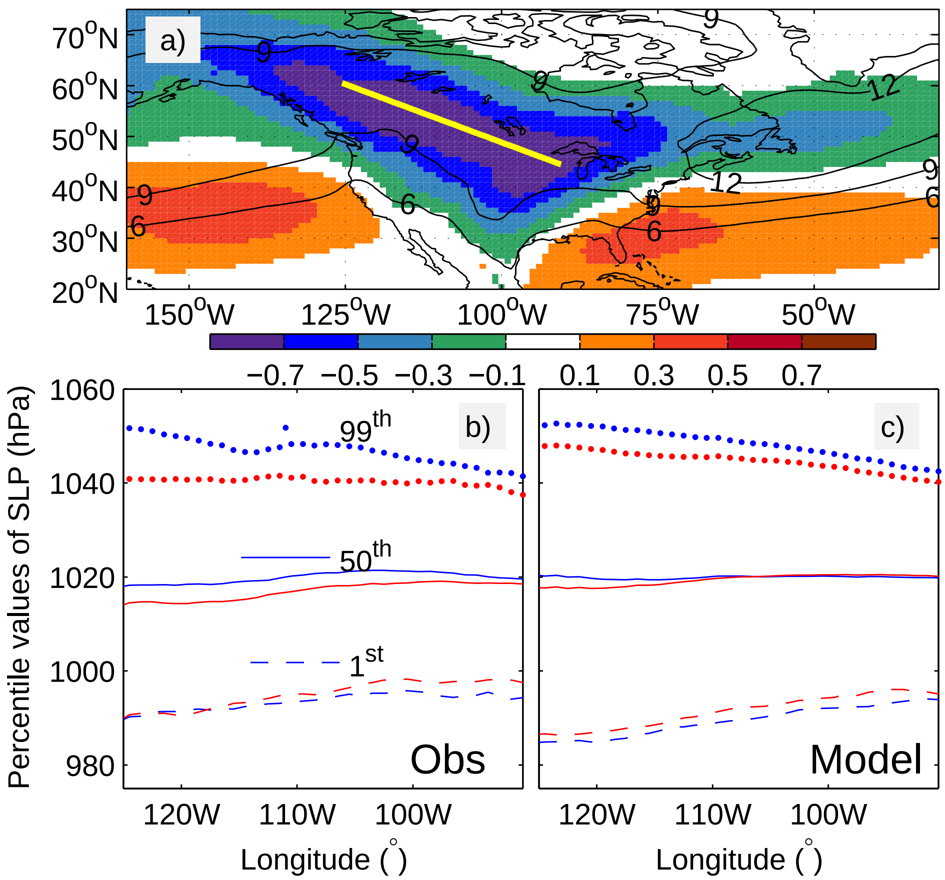

FIG. 13. a) The spatial structure of the leading predictable component (shading) that maximized the average predictability time of storm tracks in the hindcasts for the DJF season. The black contour denotes the climatological storm tracks (in hPa). The 1^{st} (dots), 50^{th} (solid) and 99^{th} (dashed) percentile values of 6-hourly SLP in the composite El Niño years (red) and La Niña years (blue) for observation b) and model c) along the crossline with maximum storm track predictable signals (the thick line in a). Note the hindcasts shown here were initialized on 1^{st} December of the composite years.

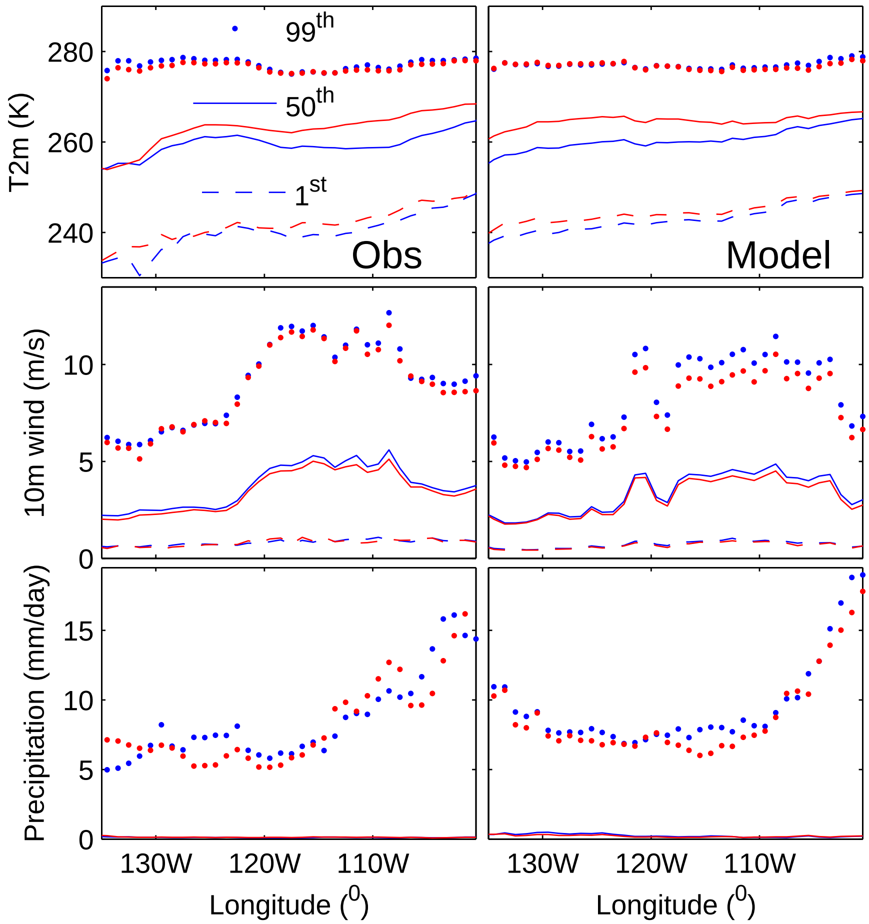

FIG. 14. The 1st (dots), 50th (solid) and 99th (dashed) percentile values of 6-hourly 2-m air temperature (top), 10-m wind speed (middle) and daily precipitation (bottom) in the composite El Niño years (red) and La Niña years (blue) for observation (left) and model (right) in the crossline with maximum storm track predictable signals (the heavy line in the upper panel of Fig. 13). Note the hindcasts shown here were initialized on 1st December of the composite years.

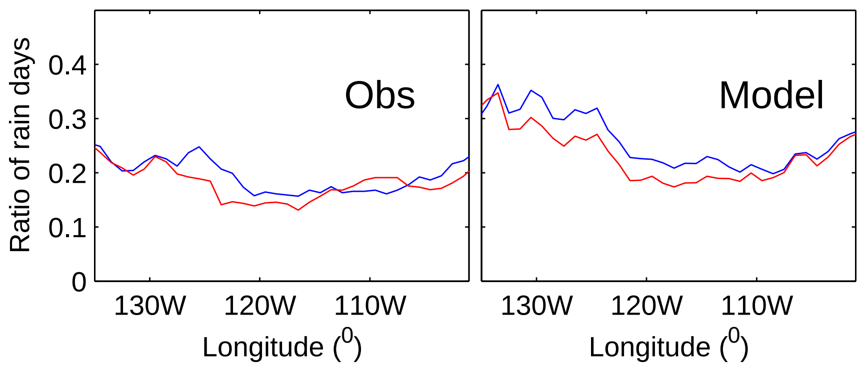

FIG. 15. The rainy day ratio during the composite El Niño years (red) and La Niña years (blue) for observation (left) and model (right) in the crossline with maximum storm track predictable signals (the heavy line in the upper panel in Fig. 13).